Molecular Basis of C–S Bond Cleavage in the Glycyl Radical Enzyme Isethionate Sulfite-Lyase

Christopher D. Dawson[1,7], Stephania M. Irwin[2,7], Lindsey R. F. Backman[3], Chip Le[2], Vyshnavi Vennelakanti[3,4], Zhongyue Yang[4], Heather J. Kulik[4*], Catherine L. Drennan[1,3,5,8*], and Emily P. Balskus[2,6*]

1. Department of Biology, Massachusetts Institute of Technology, Cambridge, MA 02139, USA

2. Department of Chemistry and Chemical Biology, Harvard University, 12 Oxford Street, Cambridge, Massachusetts 02138, USA

3. Department of Chemistry, Massachusetts Institute of Technology, Cambridge, MA 02139, USA

4. Department of Chemical Engineering, Cambridge, MA 02139 USA

5. Howard Hughes Medical Institute, Massachusetts Institute of Technology, Cambridge, MA 02139, USA

6. Broad Institute, Cambridge, MA 02139, USA.

7. These authors contributed equally

8. Lead Contact

**Corresponding authors: balskus@chemistry.harvard.edu (E.P.B.), cdrennan@mit.edu (C.L.D.), hjkulik@mit.edu (H.J.K)*

Summary

Desulfonation of isethionate by the bacterial glycyl radical enzyme (GRE) isethionate sulfite-lyase (IslA) generates sulfite, a substrate for sulfite respiration that in turn produces the disease-associated metabolite hydrogen sulfide. Here, we present a 2.7 Å resolution X-ray structure of wild-type IslA from *Bilophila wadsworthia* with isethionate bound. In comparison to other GREs, alternate positioning of the active site β strands allows for distinct residue positions to contribute to substrate binding. These structural differences combined with sequence variations create a highly tailored active site for the binding of the negatively charged isethionate substrate. Through the kinetic analysis of fourteen IslA variants and computational analyses, we probe the mechanism by which radical chemistry is used for C–S bond cleavage. This work further elucidates the

structural basis of chemistry within the GRE superfamily and will inform structure-based inhibitor design of IsIA and thus of microbial hydrogen sulfide production.

Keywords: carbon-sulfur bond cleavage, glycyl radical enzyme, isethionate, sulfite, hydrogen sulfide, microbiome

Certain gut bacteria release hydrogen sulfide as a byproduct of their respiration, which has implications for human health. Increased levels of hydrogen sulfide-producing bacteria are linked to a thinner colonic mucus barrier and multiple diseases including inflammatory bowel disease (Ijssennagger et al., 2016), Crohn's disease, ulcerative colitis (Carbonero et al., 2012; Singh and Lin, 2015), and colorectal cancer (Yazici et al., 2017). Hydrogen sulfide levels in the human body depend largely on the gut microbiome (Shen et al., 2013) and have been implicated in circulatory system homeostasis (Tomasova et al., 2016) and antibiotic neutralization (Shatalin et al., 2011). One prominent bacterial species that generates hydrogen sulfide from sulfite is *Bilophila wadsworthia*. Isolated from fecal and appendicitis specimens and named for its ability to readily digest bile (Baron et al., 1989), *B. wadsworthia* is an opportunistic pathogen (Feng et al., 2017) and the third most common anaerobic bacterium isolated from removed appendices (Baron et al., 1992). Targeting hydrogen sulfide production by *B. wadsworthia* and other gut bacteria such as sulfate-reducing bacteria (SRB) could become a therapeutic strategy to address these medical issues.

To understand hydrogen sulfide production by *B. wadsworthia* we must understand the source of sulfur (**Fig. 1A**). One critical source of sulfur is isethionate (2-hydroxyethanesulfonate, Ise), which is derived primarily from microbiome-dependent deamination of taurine, an abundant osmolyte in mammals and the second most abundant free amino acid in the human ileum and proximal colon (Smith and Macfarlane, 1998), as well as a conjugate of bile salts (Fellman et al., 1980). Recently

the enzyme responsible for catalyzing C–S bond cleavage of Ise to form acetaldehyde and sulfite, isethionate sulfite-lyase (IslA), was identified and biochemically characterized from *B. wadsworthia* (Peck et al., 2019), although isethionate lyase activity has been known for decades (Kertesz, 2000; Laue et al., 1997; Lie et al., 1999; Lie et al., 1996). IslA homologs are also found in the genomes of SRB from the human gut microbiome and other environments (Goldstein et al., 2003; Peck et al., 2019).

IslA belongs to the glycyl radical enzyme (GRE) superfamily, which performs diverse chemical reactions under anaerobic conditions (Backman et al., 2017). All characterized GREs share a 10-stranded α/β barrel architecture housing the active site, including two loops named for catalytically essential residues: the Cys loop and the Gly loop. Each GRE is activated by a dedicated radical *S*-adenosylmethionine (AdoMet)-dependent [4Fe-4S] activase (IslB for the IslA GRE) that installs a radical on a glycine residue on the Gly loop. During the reaction cycle this glycyl radical is thought to abstract a hydrogen atom from a conserved cysteine residue on the Cys loop, forming a catalytic thiyl radical (**Fig. 1B**). This thiyl radical abstracts a hydrogen atom from substrate to form a substrate radical that rearranges forming a product radical. The radical is then transferred back to the catalytic Cys and subsequently to Gly, allowing for multiple rounds of turnover.

IslA falls into the eliminase class of GREs (Peck et al., 2019), which also includes propane-1,2-diol dehydratase (PD) (LaMattina et al., 2016b), B_{12}-independent glycerol

dehydratase (GD) (O'Brien et al., 2004), *trans*-4-hydroxy-L-proline (Hyp) dehydratase (HypD) (Levin et al., 2017), and choline trimethylamine-lyase (CutC) (Craciun and Balskus, 2012). By analogy to these other GRE eliminases, we hypothesize that IslA performs C–S bond cleavage on Ise through a 1,2–elimination mechanism (**Fig. 1C**). Furthermore, CutC presents an interesting case for comparison to IslA, since their substrates are both functionalized ethanol derivatives (**Fig. S1**). Both substrates also possess charged leaving groups which present unique chemical challenges for their respective enzymes in terms of both substrate recognition and leaving group stabilization.

Recently, a crystal structure of IslA from *Desulfovibrio vulgaris* Hildenborough (DvIslA) was solved using a 23-amino acid N-terminal truncation and "surface-entropy reduction mutations" with residues 133-136 substituted with alanine residues (Xing et al., 2019), providing a first view of an IslA. Here, we present a full structure/function analysis of IslA, in which we report the first native IslA structure, the Ise-bound structure of IslA from *B. wadsworthia* 3.1.6 (IslA) at 2.70 Å resolution, along with the biochemical characterization of 14 enzyme variants. Collectively, these studies provide insight into how this enzyme performs C–S bond cleavage and into how substrate and reaction specificity are modulated in the GRE superfamily.

Results:

Overall architecture of IslA is consistent with other GRE eliminases

A structure of isethionate sulfite-lyase from *B. wadsworthia* 3.1.6 (IslA) was solved to 2.26 Å resolution by molecular replacement using CutC (PDB ID: 5FAU) (Bodea et al., 2016) as the search model (**Table 1**) with 1.84 Å RMSD to the CutC structure and 0.57 Å RMSD to the recently published DvIslA structure (PDB ID: 5YMR) (Xing et al., 2019). During model refinement, positive difference density was observed in the active site that resembled glycerol, a component of the purification buffer and cryoprotectant (**Fig. S2A**). After dialysis of the purified protein and increasing the isethionate concentration, a second IslA structure with the substrate Ise bound was obtained (**Fig. S2B-D**). This structure was solved to 2.70 Å resolution by molecular replacement with the glycerol-bound IslA structure as the search model (**Fig. 2, Table 1**).

As is the case for the core architecture of all characterized GRE eliminases (Backman et al., 2017), IslA is dimeric with each monomer having a buried active site located centrally within a barrel comprised of two five-stranded half β-barrels, anti-parallel to each other (β1-10), and surrounded by α-helices (**Fig. 2A**). This buried active site is believed to shield radical species from solvent quenching (Backman et al., 2017). In the active site are two nearby and catalytically-essential loops: the Cys loop and the Gly loop. All GREs have a C-terminal glycyl radical domain containing the Gly loop and its conserved Gly residue (Gly805 in IslA). The Cys loop includes the conserved catalytic Cys residue (Cys468 in IslA). Gly805 and Cys468 are 5.2 Å from each other **(Fig. 2C**), competent for radical transfer from Gly805 to Cys468 enabling the generation of a transient thiyl radical that initiates catalysis on the substrate.

IslA active site is tailored to bind the negatively charged substrate Ise

In the active site of the second IslA structure, electron density was observed for the substrate Ise (**Fig. 2B, S2**). A Glu residue (Glu470) hydrogen bonds with the hydroxyl group of Ise with an additional hydrogen bond being provided by the amide of Cys468 (**Fig. 3A**). Although the overall organization of IslA's active site approximates those of other GRE eliminases, unique features enable Ise specific binding. Several polar and electrostatic residues stabilize the negatively charged sulfonate group of Ise: Arg189 and Gln193 of β1, as well as Arg678 of β8 (**Fig. 3B, S2E,F**), all of which are conserved in IslA homologs but not in other GREs (**Fig. S3**). A water molecule that is present in all 4 molecules of the asymmetric unit provides another hydrogen bonding partner to the sulfonate group (**Fig. 3B**). This water molecule itself is stabilized by a solvent pocket located peripherally to the sulfonate group. Overall, hydrogen bonding and electrostatic interactions form a unique active site to accommodate a highly charged, hydroxyl-containing molecule like Ise (**Fig. 3C, D**).

Ise positioning in IslA is unique among GRE eliminases

A conserved feature of GRE eliminases is the CXE motif of the Cys loop (Cys468-Ile469-Glu470 in IslA) (**Fig. 2C**). Here, as in all prior GRE eliminase structures (Backman et al., 2017), the substrate sits above the Cys loop (**Fig. 2C**) and the Glu residue of the CXE motif appears to hydrogen bond with a hydroxyl group of substrate (**Fig. 3A,C**). However, in comparison to CutC (Bodea et al., 2016) and HypD (Backman

et al., 2020), the position of Ise is shifted and the orientation of the hydroxyl of Ise relative to the carboxylate of Glu470 is also shifted in order to accommodate the unique position of Ise (**Fig. 4A-D**). If the orientation of Glu470 mimicked that of the Glu residues in other GRE eliminases, it would crash into the Ise substrate (**Fig. 4D**). Even though Ise and choline are more structurally similar to each other than either is to Hyp, it is the active site of IsIA that is the outlier. Another difference generated by the unique Ise positioning is that the *pro-R* hydrogen of C2, rather than the *pro-S* hydrogen, is closer to the thiol of Cys468, with distances of 2.6 Å and 4.2 Å, respectively (**Fig. 4A, S2E**). Attempts to re-position Ise such that the pro-S hydrogen of C2 is closer to Cys468 result in a poor fit to the electron density (**Fig. S2F**). In contrast, in most other structurally characterized GRE eliminases, the thiol of the catalytic cysteine residue is closer to the *pro-S* hydrogen atom.

Another common feature of GRE active sites is that an aromatic residue packs against the substrate (Backman et al., 2017). In CutC, Phe395 provides cation-π interactions to the positively charged choline, and similarly in HypD, Phe340 is positioned to make cation-π interactions with the amino group of Hyp (**Fig. 4B,C**). Interestingly, an unexpected feature of IsIA is the presence of a Trp residue (Trp374) in the position typically occupied by Phe. Trp374 is too far (~6 Å) to directly interact with substrate, but due to its larger size, it does sit closer to Gly805 and Cys468 than is common (**Fig. 4A-D**). Although an aromatic residue is typically found in this position, only IsIA enzymes have Trp among GRE eliminases, and within the putative IsIA enzyme family, Trp374 is

conserved (**Fig. S3**). Although the role of Trp in IslA is unknown, the presence of Trp versue Phe does allow for an additional hydrogen bond between the Trp side chain and the glycyl radical loop (**Fig. 3A**), which could regulate the movement of the glycyl radical loop out of the active site for glycyl radical formation.

Alterations in barrel architecture modulate substrate specificity

In GREs, substrate-binding residues are introduced into the active site by the β strands, and when the strands adopt even subtly different orientations, the effect on the active site can be substantial (**Fig. 4E-G**). Specificity in GREs is thus determined both by the substitution of residues on similarly positioned parts of β strands and by the active site alterations created by β strands re-positioning. The biggest rearrangement of a β strand in IslA is found in β6, which allows Ise to bind in a much higher up position in the active site than those of Hyp or choline in their respective enzymes (see above). In CutC (Bodea et al., 2016) and HypD (Backman et al., 2020), β6 runs closer to the active site, positioning Tyr506 and Tyr450, respectively, toward substrate (**Fig. 4F,G**). In IslA, β6 departs the active site more abruptly, creating a water binding site and room for substrate Ise to sit higher in the active site (**Fig. 4E**). To secure Ise in this "higher" substrate-binding position, Arg678 extends into the active site from a position on β8 too distant to interact with substrate in CutC and HypD. Arg678 appears to be important in making a favorable electrostatic interaction with the substrate sulfonate group. β8 of IslA also contributes Phe682, which occupies a similar space as a β3 residue in CutC (Phe389), fulfilling a van der Waals packing role with the same type of residue from a

189 different strand. In contrast, in HypD the corresponding residues to Phe682-IslA and
190 Phe389-CutC are Thr645 and Ser334, both hydrogen bond donors to substrate Hyp.
191
192 Strands β1 and 2 also contribute residues to the active sites of all three of these GRE
193 enzymes (**Fig. 4E-G**). Like β6, the conformation of β2 can be quite different in different
194 GRE eliminases (**Fig. 4E-G**). Also, the importance of β2 residues to substrate binding
195 and/or catalysis can differ considerably. An essential catalytic residue in HypD is
196 contributed by β2 (Asp278) (Backman et al., 2020), whereas IslA-Thr312 and CutC-
197 Thr334 do not directly contact substrate (**Fig. 4E-G**). In CutC, a different (lower)
198 conformation of β2 positions Thr334 too far from substrate, whereas in IslA, a different
199 (higher) position of substrate puts Thr312 out of reach (**Fig. 4E-G**). It is clear from
200 comparing structures of eliminases that the flexibility of GRE active sites is quite
201 substantial.
202
203 Finally, β1 residues appear to be key players in all three enzymes. A common site is
204 employed that contributes substrate-interacting residues: IslA-Gln193, CutC-Asp216,
205 and HypD-His160 (**Fig. 4E-G**). In contrast, the site on β1 of CutC that provides
206 substrate-binding residue Tyr208 is not used by either HypD or IslA, but both HypD and
207 IslA use an upstream site to contribute an Arg residue. Although this Arg (IslA-Arg189
208 and HypD-Arg156) is from the same position on the backbone, the side chain
209 orientations are quite different. IslA-Arg189 swings to interact directly with Ise, whereas
210 HypD-Arg156 interacts indirectly with Hyp through a water molecule. Overall, comparing

IslA, CutC (Bodea et al., 2016), and HypD (Backman et al., 2020) showcases the extraordinary ability of GREs to tailor interactions with different substrates using the same GRE β barrel architecture.

A similar putative substrate channel is found in several GRE structures

The active sites of GREs are relatively buried, which serves to protect the radical species from oxygen damage. Due to the buried nature of the active site, substrate access channels and product release channels are required. The clearest example of a substrate channel is found in the GRE benzylsuccinate synthase (BSS) (Funk et al., 2014; Funk et al., 2015), which must accommodate entry of a volatile and hydrophobic aromatic compound, toluene, as well as a polar molecule, fumarate. BSS has accessory subunits that are required in addition to the catalytic α subunit, a feature shared with another characterized GRE, 4-hydroxyphenylacetate decarboxylase (HPAD; PDB ID: 2Y8N) (Martins et al., 2011). In the BSS-αβγ structure (PDB ID: 4PKF) (Funk et al., 2014; Funk et al., 2015), a hairpin loop of a non-catalytic subunit (BSS-β) plugs the putative substrate access channel in the catalytic subunit (BSS-α), closing off the active site once substrate is bound (**Fig. S4A,B)**. Thus, the structures of the open BSS-αγ and closed BSS-αβγ enable us to visualize substrate channel closure in a GRE.

To investigate whether other GREs have a similar channel to that of BSS, we ran an analysis of available GRE structures using the program CAVER 3.0 (Chovancova et al., 2012) and compared channels identified to the toluene channel of BSS (**Fig. 5**). We find

an equivalent channel to that in BSS in the two glycerol-bound structures of HypD and IslA (**Fig. 5**). Furthermore, this putative channel is also seen in the substrate-free structure of HPAD-αγ (Martins et al., 2011). The lengths of these channels range between 14 Å and 19 Å from the active site to the protein surface. Residues along the channels are highly conserved in each of these four GREs, consistent with these channels playing a functional role (**Fig. S4C-F**). Considering the many architectural differences among these GREs, a consistent channel is an interesting feature worthy of further experimental validation.

Site-directed mutagenesis experiments validate Ise-coordinating residues as playing roles in substrate binding and catalysis

Using our structural data, we sought to probe the roles of active site residues through site-directed mutagenesis experiments. We sought first to validate that Gly805 forms the glycyl radical and that Cys468 is catalytically essential by generating G805A and C468S variants of IslA. Unsurprisingly, EPR spectroscopy of the G805A variant detects no glycyl radical species (**Table 2, Fig. S5**). The C468S variant can form a glycyl radical but has no detectable sulfite release in an endpoint assay (**Fig. S5C,D**), as expected considering its predicted role in catalysis.

Next, we examined residues observed to interact with Ise in the crystal structure. We made variants of IslA to disrupt putative interactions with the hydroxyl group of Ise (E470Q) and the sulfonate moiety of Ise (Q193A, R189E, R678E, R189E/R678E). All

five enzyme variants were activated by IslB to some extent, with R189E having the greatest glycyl radical content (**Table 2**). However, none of the five variants displayed endpoint activity (**Fig. S5C,D**).

We also investigated the aromatic residues in the active site (F682A, F682Y, W374F and W374Y) (**Fig. 2B,C**). IslB successfully installed a glycyl radical into these enzyme variants as determined by EPR spectroscopy, and the endpoint assay indicated turnover (**Table 2, Fig. S5C,D**). To determine the effects these mutations have on catalysis, kinetic assays were conducted for wild type IslA and the IslA variants F682A, F682Y, W374F and W374Y. The K_M values for the wild type *Bilophila wadsworthia* IslA are modest compared to other GREs such as CutC (0.13 mM) or HypD (1.2 mM) (Bodea et al., 2016; Levin et al., 2017), but comparable to the other published IslA K_M values from *Desulfovibrio desulfuricans* DSM642 (6.3 mM) and *Desulfovibrio vulgaris* Hildenborough (44.8 mM) (Peck et al., 2019; Xing et al., 2019) and to the K_M value for the recently discovered C–S bond-cleaving GRE, HpsG (13 mM) (Liu et al., 2020). The catalytic efficiencies of each of the IslA variants F682A, F682Y, W374F and W374Y were 1-2 orders of magnitude lower than wildtype IslA due largely to decreased k_{cat} with little difference in K_M, suggesting these amino acids play a larger role in catalysis than in substrate binding. Phe682 appears to be important for catalysis, perhaps through controlling the substrate conformation, though it is not necessary for Ise cleavage. Trp374 is closer to the catalytic cysteine (3.5 Å from the thiol of Cys468) and the glycyl radical (3.5 Å from the carbonyl of Gly805) than to substrate (~6 Å). The side chain of

277 Trp374 is within hydrogen bond distance of the carbonyl of Ala804 **(Fig. 3A**), providing
278 a direct interaction to the Gly loop. Interestingly, W374F and W374Y variants display
279 more glycyl radical content than WT but are less active (**Table 2**). It could be that the
280 lost of the hydrogen bond to the Gly loop through residue substitution increases the
281 dynamics of the Gly loop, and the results of increased dynamics are two-fold. Activation,
282 which requires Gly loop movement, is increased whereas, radical transfer between Gly
283 to Cys, which requires a close positioning of the Gly loop to Cys, is impaired.
284
285 Finally, we mutated additional residues Ile192 and Val680. Ile192 is near the sulfonate
286 group of the Ise substrate, whereas Val680 is located ~5 Å from Ise but in close
287 proximity (~3 Å) to the catalytically important Cys468 (**Fig. 2B,C**). I192A was found to
288 have nearly identical radical installation to the wild-type, and a similar K_M with a
289 decreased k_{cat} **(Table 2)**. However, this mutant had the highest k_{cat} of the panel of
290 mutants assayed, suggesting it is less critical for catalysis. This finding is further
291 supported by its lack of conservation among IslA homologs (**Fig. S3**). Surprisingly,
292 V680A was found to have the maximal amount of glycyl radical installation of the
293 assayed mutants despite being inactive toward Ise. It is unclear if this increase in glycyl
294 radical activation for this variant or others is due to altered interaction between the
295 activase and IslA or to altered stability of the Gly radical. Further investigation is needed
296 to determine the role of this residue, but this finding highlights how small structural
297 changes relatively far from the substrate can dramatically impact catalysis.
298

Deuterium-labeling studies show that the abstracted hydrogen atom is returned to the substrate

To better understand the mechanism of IslA, we performed deuterium-labeling studies to determine if the hydrogen atom abstracted from Ise is returned to the product or is lost to solvent quenching or exchange. We incubated activated IslA with either unlabeled or 2,2-d_2-Ise in a coupled assay with yeast alcohol dehydrogenase (YADH) to generate ethanol as a final product (**Fig. 6A**). Gas chromatography-mass spectrometry (GC-MS) analysis using positive chemical ionization (PCI) revealed the formation of di-deuterated ethanol (**Fig. 6B,C**). GC-MS with electron impact ionization (EI) was used to assign this product as 1,2-d_2-ethanol (**Fig. 6B,C**). These observations are consistent with the deuterium abstracted from 2,2-d_2-Ise returning to the product during catalysis. The absence of a singly-deuterated ethanol product also indicates a lack of deuterium exchange with solvent.

Discussion:

The structure of WT IslA from *Bilophila wadsworthia* with Ise bound has allowed us to compare how this GRE binds substrate with how other GRE eliminases position their substrates for catalysis. We find that IslA positions substrate higher in the active site than is typical for GREs that perform similar heteroatom elimination reactions. This higher positioning enables interactions with Arg678 and Arg189, which serve to counter the negative charge of the Ise sulfonate group. Interestingly, the unique binding position of Ise is not due solely to the identity of residues in the active site; the positioning of β

strands of the 10-stranded barrel is also different, allowing residues from atypical positions on these strands to contribute to the active site. The combination of the repositioning of β strands with residue substitutions adds to the malleability of the active sites of GRE enzymes such that a higher degree of tailoring is possible. This malleability also leads to difficulty in bioinformatically predicting the types of chemistry and substrates a GRE of unknown function might perform, highlighting the critical need for structural characterization.

We can also compare the binding mode of Ise with that of other sulfonate compounds. In the Protein Data Bank, we find multiple sulfonate-containing compounds bound to proteins, including molecules derived from crystallization conditions that are adventitiously bound to proteins and enzyme inhibitors that are bound to their target enzymes (**Fig. S6A**). Physiologically relevant bound sulfonates are restricted to the following metabolites: Ise, taurine, and sulfolactate (**Fig. S6B**). A survey of sulfonate binding modes suggests that common strategies include the use of water molecules, backbone amides, or arginine and asparagine residues to form hydrogen bonds and electrostatic interactions (DiDonato et al., 2006; Nishiyama et al., 2016; O'Brien et al., 2003; Rossocha et al., 2005; Xing et al., 2019; Zhou et al., 2019). Unique to IslA is a binding mode that provides a glutamine residue and two arginine residues to coordinate the sulfonate moiety. The way IslA binds Ise is not only distinct among GRE eliminases but also unique among sulfonate binding proteins.

The radical-based cleavage of Ise would be expected to occur via either a direct elimination reaction or via a migration reaction. Based on biochemical and computational data for CutC and GD, these enzymes have been proposed to perform direct elimination chemistry (Bodea et al., 2016; Feliks and Ullmann, 2012; Kovačević et al., 2018; O'Brien et al., 2004; Yang et al., 2019). In contrast, the adenosylcobalamin-dependent ethanolamine ammonia-lyase (EAL) has been proposed to perform a radical-based migration reaction (Toraya, 2003). Comparing the placement of residues in the active sites of CutC, EAL and IslA shows that CutC and IslA active sites contain residues that would appear to sterically prevent migration chemistry (Gln193 and Thr312 in IslA and Thr502 in CutC), whereas EAL has a residue to facilitate migration (Glu287) (**Fig. S7**) (Bodea et al., 2016; Mori et al., 2014; Shibata et al., 2010; Toraya, 2003). Using this structural analysis along with our biochemical data, we propose a mechanism for IslA that involves direct elimination of the sulfonate moiety of Ise to generate acetaldehyde and sulfite. After substrate binding, during the catalytic cycle, the glycyl radical abstracts a hydrogen atom from Cys468 forming a thiyl radical (**Fig. 6D, step I**). Based on the fit to the electron density of Ise (**Fig. S2E,F**) and distances from the thiol of Cys468 to hydrogen atoms on C2 of Ise, we predict thiyl radical hydrogen atom abstraction at the *pro-R* position (**Fig. 4A; Fig. 6D, step II**), in contrast to most other GRE eliminases, which are proposed to abstract the *pro-S* hydrogen atom of substrate based on structural, biochemical and computational data (Backman et al., 2020; Bodea et al., 2016; Feliks and Ullmann, 2012; Kovačević et al., 2018; LaMattina et al., 2016a, b; O'Brien et al., 2004; Yang et al., 2019). However, the structure of a

newly characterized C–S-cleaving GRE HpsG also predicts abstraction of the corresponding sterochemically positioned hydrogen atom of its substrate, suggesting this could be a common feature of this group of GREs (Liu et al. 2020). Accompanying this hydrogen atom abstraction, we propose a deprotonation of the hydroxyl of Ise facilitated by Glu470 (**Fig. 6D, step II**) as is proposed for CutC (Bodea et al., 2016) and consistent with complete loss of activity in the E470Q variant. Further supporting this proposal, high-level QM calculations on substrate models with the enzyme environment approximated by dielectric screening show that the presence of an acetate molecule (representing the Glu470 side chain) stabilizes the transition state for C–H bond abstraction by 3.8 kcal/mol (**Fig. 6E, Table S1-3**). This unstable, transient ketyl radical species decomposes resulting in C–S bond cleavage and the generation of the sulfite product (**Fig. 6D, step III, IV, V**). The resulting radical species rearranges and abstracts a hydrogen atom from Cys468 to regenerate the thiyl radical and to produce the acetaldehyde product, as supported by the deuterium-labeling experiments (**Fig. 6D, step V, VI**). The thiyl radical abstracts a hydrogen atom from glycine to reform the glycyl radical for the next round of catalysis (**Fig. 6D, step VII**). The products, acetaldehyde and sulfite, are released, potentially through a highly conserved channel seen in IslA and other GREs (**Fig. 5**), allowing for the next Ise to bind. Thus, IslA employs radical-based chemistry to break a carbon-sulfur bond of a sulfonate group, the first such example of this reactivity among enzymes.

This structural and biochemical analysis of IslA has enabled us to identify residues important for substrate binding and catalysis to explore how an opportunistic pathogen extracts sulfite from host-derived metabolites to fuel respiration. These data will aid in the identification of GREs as putative IslA enzymes and will enable drug design efforts towards reducing the negative effects of microbially-derived hydrogen sulfide. Using IslA, microbes have devised a way to extract sulfite from a sulfonate common in biological systems potentially to the detriment of their hosts.

Significance

An overabundance of hydrogen sulfide released during sulfite respiration by the gut microbiome is associated with diseases in the human host. The recently discovered glycyl radical enzyme isethionate sulfite-lyase (IslA) enables microbes to extract sulfite from isethionate, a derivative of the abundant metabolite taurine. Here, we identify residues important for binding and catalysis to expand our mechanistic understanding of IslA-mediated C–S cleavage toward the ultimate goal of structure-based inhibitor design of IslA and thus of hydrogen sulfide production.

Acknowledgements

We thank Spencer Peck for help with protein purification and biochemistry, and Mary Andorfer for help with the EPR spectroscopy. This work was supported in part by the National Institutes of Health (NIH) Grant R35 GM126982 (C.L.D), the NIH Pre-Doctoral Training Grant T32GM007287 (C.D.D.), the National Science Foundation (NSF)

Graduate Research Fellowship under Grant No. 1122374 (L.R.F.B.), and the NSF under CBET-1704266 (H.J.K. and V.V.). C.L.D. is a Howard Hughes Medical Institute (HHMI) Investigator. L.R.F.B. is a recipient of a Dow Fellowship at MIT and a Gilliam Fellowship from HHMI. The work was also funded by the Bill & Melinda Gates Foundation (Howard Hughes Medical Institute-Gates Faculty Scholar Award) (to E.P.B), the NSERC Postgraduate Scholarship Doctoral Program (to S.M.I), the Sir James Lougheed Award of Distinction (to S.M.I), and a Career Award at the Scientific Interface from the Burroughs Wellcome Fund (to H.J.K., Z.Y., and V.V.). This work was completed in part with resources at the MIT Department of Chemistry Instrumentation Facility with the help of John Grimes, and the Harvard Center for Mass Spectrometry. In addition, this work is based upon research conducted at the Northeastern Collaborative Access Team beamlines, which are funded by the NIH (P30 GM124165). The Pilatus 6M detector on 24-ID-C beam line is funded by a NIH-ORIP HEI grant (S10 RR029205). This research used resources of the Advanced Photon Source, a U.S. Department of Energy (DOE) Office of Science User Facility operated for the DOE Office of Science by Argonne National Laboratory under Contract No. DE-AC02-06CH11357.

Author Contributions

C.D.D. performed crystallization, X-ray data collection, and structure determination. S.M.I. purified proteins and carried out all biochemical assays. C.D.D. and S.M.I. analyzed structures and biochemical data with input from E.P.B. and C.L.D. C.L.

performed chemical synthesis. V.V., Z.Y., and H.J.K. conducted computational studies.

C.D.D., S.M.I., L.R.F.B, E.P.B., and C.L.D. wrote the manuscript.

Declaration of Interest

The authors declare no competing interests.

Figure Titles and Legends

Fig. 1: IslA-mediated anaerobic metabolism of organosulfonates by intestinal bacteria releases the disease-associated metabolite hydrogen sulfide (H_2S). (A) Deamination of taurine by human gut microbes yields isethionate (Ise), which is cleaved and reduced to H_2S in microbial respiration. (B) The activating enzyme for IslA, IslB, installs a glycyl radical on a particular glycine residue of IslA using Radical SAM chemistry, i.e. the formation of a 5'-deoxyadenosyl radical (Ado•) species from the reductive cleavage of *S*-adenosylmethionine (AdoMet) using a [4Fe-4S] cluster. The glycyl radical (Gly•) transiently forms the catalytically essential thiyl radical species (Cys•). (C) Proposed reaction scheme for IslA. Radical species are shown in red.

Fig. 2: Overall architecture of *Bilophila wadsworthia* isethionate sulfite-lyase (IslA) (A) IslA dimer contains an active site comprised of two-five stranded half barrels enclosing substrate, the Cys loop (purple) and the Gly loop (yellow). Shown in spheres are Ise, the catalytic cysteine and glycine residues. (B) Active site views of substrate interacting residues with F_o-F_c composite omit map contoured to 1.5σ around Ise. (C) Active site view with proposed H atom abstraction route shown in red.

Fig. 3: Ise binding mode in IslA. (A) Residues and water molecules interacting with Ise hydroxyl group and Gly loop shown as dotted lines and waters shown as red spheres. (B) Residues and water molecules interacting with Ise sulfonate group. (C) Simplified active site view (D) Active site hydrogen bond interaction scheme.

Fig. 4: Substrate positioning and active site architecture differs among GRE eliminases. (A) IslA shown in green with proposed radical transfer pathway shown as a red dotted line from the catalytic Cys (Cys468) to the closest substrate carbon marked with a red star. The white dotted line indicates the distance between the more distant hydrogen of the substrate carbon. (B) CutC (PDB ID: 5FAU) shown in pink. (C) HypD (PDB ID: 6VXE) shown in teal. (D) Overlay of A-C. (E) IslA with substrate, Gly loop, Cys loop, β1, β2, β3, β6, and β8 shown as pink, yellow, purple, blue, green, brown, orange, and red, respectively. Arrows highlight particularly different beta strands. (F) CutC (PDB ID: 5FAU) colored as in A. (G) HypD (PDB ID: 6VXE) colored as in A.

Fig. 5: Several putative GRE substrate channels share a similar location. IslA dimer shown in green and a boxed monomer that shares the orientation with the other enzyme monomers that are shown. BSS (PDB ID: 4PKC) α subunit (brown), HypD (PDB ID: 6VXE) (teal), HPAD (PDB ID: 2Y8N) α subunit (red) are all shown in transparency with channels identified using CAVER 3.0 shown opaque.

Fig. 6: Assay with stable-isotope-labeled Ise provides insights into the mechanism of IslA. (A) Schematic of the biochemical assay with GC-MS detection. (B) Potential positive chemical ionization (PCI) ions to determine total deuterium incorporation and potential electron impact (EI) ions used to identify the location of the deuterium atoms. (C) MS data from GC-MS assays. The enzymatic reaction with 2,2-d_2-isethionate generates 1,2-d_2-ethanol as the only detectable deuterated product. Unlabeled ethanol (m/z = 47.0491) and d_2-ethanol (m/z = 49.0617) are detected via PCI when IslA reacts with 2,2-d_2-Ise. Using EI ionization and 2,2-d_2-Ise as a substrate for IslA, the ion at 47.0460 represents di-deuterated ethanol. There is a +1 shift of the 31.0179 fragment ion of this product to 32.0241, indicating only a single deuterium is on the C1 fragment, as double-deuterated 33.0304 is not observed. We have located this deuterium to the C, rather than the O, since the O-H bond is generated via the YADH-NADH coupled reaction that is run in water-based buffer. Thus the 46.0398 ion arises from a loss of deuterium due to ionization and does not correspond to 1-d_1-ethanol. The reaction of IslA with unlabeled isethionate generates unlabeled ethanol (m/z = 45.0335 and 31.0179). When boiled enzyme is mixed with d_2-isethionate, unlabeled ethanol is present in the background. These assays were performed in triplicate, and a representative spectrum is shown. (D) Proposed 1,2–elimination mechanism of IslA. During the catalytic cycle, the glycyl radical (Gly805) abstracts a hydrogen atom from Cys468, forming a thiyl radical (I, II). This thiyl radical abstracts the *pro-R* hydrogen atom from C2 of Ise. Glu470 deprotonates the hydroxyl group of Ise to form a transient substrate ketyl radical species (III, IV). This unstable intermediate decomposes, resulting in C–S bond cleavage and release of sulfite (V). The resulting radical species then abstracts a hydrogen atom from Cys468 to produce the second product, acetaldehyde (VI, VII). Arrows are shown in red. Hydrogen bonds are shown in dashed black. (E) Schematic of the local coupled cluster quantum mechanical calculations of C–H abstraction both with and without an acetate molecule present in a dielectric medium.

Tables with Titles and Legends

Data name	Glycerol Bound-IslA	Ise Bound-IslA
Data collection		
Wavelength (Å)	0.9792 Å	0.9792 Å
Space group	$P2_12_12$	$P2_12_12_1$
Cell dimensions		
a, b, c (Å)	119.99 132.86 107.72	130.95 163.75 181.65
Resolution (Å)	50-2.26 (2.34-2.26)†	50-2.70 (2.80-2.70)
No. of unique reflections	80740 (6838)	107420 (10625)
R_{sym} (%)	17.3 (49.5)	22.6 (102.4)
$\langle I \rangle / \langle \sigma(I) \rangle$	10.1 (2.0)	7 (1.4)
Completeness (%)	98.4 (84.8)	98.9 (99.2)
Redundancy	7.3 (3.2)	4.1 (3.8)
CC1/2	98.9 (68.1)	96.9 (49.6)
Refinement		
Resolution (Å)	50-2.26	50-2.70
No. of unique reflections	80669	107297
R_{work}/R_{free}‡	0.166/0.198	0.184/0.223
No. Atoms	13773	27303
Protein	13174	26332
Glycerol	12	
Isethionate		28
Water	587	943
B-factors Å^2 (overall)	26.0	36.7
Protein	26.4	36.8
Glycerol	23.2	
Isethionate		31.5
Water	27.0	34.5
Rmsd		
Bond Lengths (Å)	0.003	0.004
Bond Angles (°)	0.589	0.623
Rotamer outliers	1.2 %	0.94 %

† Highest resolution shell shown in parenthesis

‡R_{free} was calculated with 5% of the data

Table 1: Crystallographic Data and Refinement Statistics

Protein	Radicals per Polypeptide (%)	Detectable activity (sulfite)	K_M (mM)	k_{cat} (s^{-1})	Glycyl-radical normalized k_{cat} (s^{-1})	Catalytic efficiency using normalized k_{cat} (s^{-1} M^{-1})
Wild-type	20.8 ± 0.5	Yes	8 ± 2	2.0 ± 0.1	9.5 ± 0.6	1200 ± 310
G805A	0	No	ND	ND	ND	
C468S	22.1 ± 0.4	No	ND	ND	ND	
E470Q	11.2 ± 0.7	No	ND	ND	ND	
Q193A	17 ± 1	No	ND	ND	ND	
R189E	28.1 ± 0.6	No	ND	ND	ND	
R678E	5.9 ± 0.1	No	ND	ND	ND	
R189E/ R678E	11 ± 1	No	ND	ND	ND	
F682A	11 ± 1	Yes	6.8 ± 0.6	0.0171 ± 0.0004	0.154 ± 0.004	23 ± 2.1
F682Y	32.2 ± 0.8	Yes	8 ± 1	0.0074 ± 0.0003	0.023 ± 0.001	2.9 ± 0.4
W374F	47 ± 2	Yes	11 ± 1	0.063 ± 0.003	0.133 ± 0.006	12 ± 1.2
W374Y	30.2 ± 0.9	Yes	16.0 ± 0.9	0.140 ± 0.003	0.465 ± 0.009	29 ± 1.7
I192A	21 ± 1	Yes	12 ± 2	0.40 ± 0.02	1.9 ± 0.1	160 ± 28
V680A	52 ± 3	No	ND	ND	ND	

Table 2: Activation and kinetics of IslA variants from reactions repeated in triplicate. Radicals per polypeptide indicate mean ± standard deviations; kinetic parameters are listed as mean ± standard error.

STAR Methods

RESOURCE AVAILABILITY

Lead Contact

Further information and requests for resources and reagents should be directed to and will be fulfilled by the Lead Contact, Catherine Drennan (cdrennan@mit.edu).

Materials Availability

Plasmids generated in this study will be made available upon request.

Data and Code Availability

The structural data sets generated in this study are available at the Protein Data Bank (PDB ID: tk, tk). The published article includes all biochemical data generated and analyzed in this study. The QM initial and optimized geometries are provided in the Supporting Information.

EXPERMENTAL MODEL AND SUBJECT DETAILS

Bacterial Culturing Conditions

E. coli TOP10 and *E. coli* BL21(DE3) cultures were grown at 37 °C in Luria-Bertani (LB) broth. Induction of protein expression for *E. coli* BL21(DE3) cultures took place at 15 °C. *E. coli* BL21(DE3) ΔiscR cultures were grown at 37 °C in LB broth supplemented with glucose (1% w/v), Fe(III)-ammonium-citrate (2 mM), cysteine (2 mM) and sodium fumarate (20 mM). Induction of protein expression took place at 15 °C under N_2 atmosphere.

METHOD DETAILS

Chemicals

All chemicals and reagents were of the highest purity available and purchased from Sigma-Aldrich unless otherwise indicated. Luria-Bertani (LB) medium was obtained from

Alfa Aesar. Isopropyl β-D-1-thiogalactopyranoside (IPTG) was purchased from Teknova (Hollister, CA). Glycerol was purchased from VWR. N-(9-acridinyl)maleimide was purchased from TCI America. SDS-PAGE gels were purchased from Invitrogen. Crystallization reagents were purchased from Hampton Research.

Plasmid Construction

The wildtype pET-28a-IslA and pET-29b-IslB plasmids were prepared as described previously (Peck et al., 2019). Site-directed mutagenesis of IslA was performed one of two ways using the corresponding oligonucleotides listed in **Table S4**. For Q193A, C468S, E470Q, and G805A, a three-piece Gibson Assembly was performed using previously reported conditions for assembling the WT-IslA plasmid (Peck, et al. 2019). For the majority of constructs, PCR reactions of 25 μL contained 12.5 μL of Phusion High-Fidelity PCR Master Mix (New England Biolabs), 50 ng of pET-28a-IslA template, 0.5 μL DMSO and 0.25 μM of each primer. Thermocycling was carried out in a C1000 Gradient Cycler (Bio-Rad) using the following parameters: denaturation for 2 min at 98 ˚C, followed by 22 cycles of denaturation for 30 s at 98 ˚C, annealing for 30 s at 55-65 ˚C (depending on construct), and extension for 8 min at 72 ˚C, followed by a final extension for 10 min at 72 ˚C. Digestion of the methylated template plasmid was performed with Dpn1 (NEB), and 2 μL of each digestion was used to transform 50 μL chemically competent *E. coli* TOP10 cells by incubating them on ice for 2 min, incubating the cells and DNA at 42 ˚C for 30 s, and recovering on ice for 1 min; LB medium (500 μL) was added and the cells were incubated at 37 ˚C for 1.5 h. The cells

were plated on LB supplemented with kanamycin (50 µg/mL, hereafter referred to as LB-Kan50) and then grown at 37 ˚C overnight. Individual colonies were inoculated into 5 mL LB-Kan50 and grown overnight at 37 ˚C. The plasmids were isolated using an E.Z.N.A. Plasmid Mini Kit I (Omega Bio-tek). The identities of each of the resulting plasmids were confirmed by sequencing the purified plasmid DNA (Eton Biosciences).

Protein Expression and Purification

The expression host *E. coli* BL21(DE3) ΔiscR for expression of IslB was constructed as described previously (Peck et al., 2019). Proteins were purified as described previously, with modifications noted below (Peck et al., 2019). For heterologous overexpression, 50 ng of plasmid was transformed into 50 µL chemically competent *E. coli* BL21(DE3) (for IslA), or chemically competent *E. coli* BL21(DE3) ΔiscR (IslB) as above. Cells were plated on LB-Kan50 and grown overnight and single colonies were inoculated into 25 mL LB-Kan50.

For expression of IslA and IslB, a 25 mL starter culture was inoculated into 2 L LB-Kan50 in a 4 L shake-flasks for the IslA, or into 2 L LB-Kan50 in a 2.8 L baffled screw top flask for IslB. IslB medium was supplemented with glucose (1% w/v) and Fe(III)-ammonium-citrate (2 mM). The cultures were grown at 37 ˚C until they reached an OD_{600} of ~0.6 and IPTG (0.3 mM) was added. The temperature was lowered to 15 ˚C and the cultures incubated overnight. At the point of induction, the cultures expressing IslB were additionally sparged with N_2 for 20 min, and cysteine (2 mM) and sodium

fumarate (20 mM) were added, before the cultures were sealed with screw-cap tops and electrical tape and incubated overnight at 15 ˚C without shaking.

For the preparation of IslB, all subsequent steps took place at 4 ˚C in an anoxic chamber unless otherwise specified (centrifugation and incubation on a nutator). After overnight growth, the cells were harvested by centrifugation (6,770 g, 10 min). The supernatant was decanted, and the cells were resuspended in 35 mL lysis buffer. For IslA, the lysis buffer was 50 mM HEPES pH 7.5, 200 mM NaCl, 20 mM imidazole, and for IslB the same buffer was supplemented with lysozyme (8 mg), half of an EDTA-free protease inhibitor tablet and DTT (5 mM). For IslA, the cells were lysed by sonication with a ½" horn (6 min total sonication, 10 s on, 30 s off, 25% amplitude, Branson Ultrasonics). The lysates were clarified by centrifugation (30 min, 20,000 g). For IslB, the cells were first incubated with the lysozyme at 4 ˚C for 1 h then lysed by sonication with a ½" horn (7 min total sonication, 10 s on, 30 s off, 25% amplitude), and the lysates were clarified by centrifugation (20,000 g, 30 min).

The supernatant was incubated with 3 mL Ni-NTA resin (Qiagen) that had been equilibrated with 10 column volumes of the respective lysis buffer for 1 h. The resin was pelleted (500 g, 5 min), the supernatant was decanted, and the resin was transferred into a column. After the flowthrough was collected, the resin was washed with 50 mL lysis buffer. The proteins were eluted by sequential washes with elution buffer (50 mM HEPES pH 7.5, 200 mM NaCl, 250 mM imidazole); for IslA, this was one step with 12

602 mL each, for IslB three steps of 4 mL. SDS-PAGE was used to identify the fractions
603 containing the proteins and their purity. Purified proteins were loaded into a dialysis
604 cassette of an appropriate size; 20 kDa MWCO for IslA, and 10 kDa for IslB (Thermo
605 Fisher Scientific).
606
607 For endpoint assays, EPR, kinetic analysis and labeling studies, the proteins were
608 dialyzed three times against 1.3 L dialysis buffer (50 mM HEPES pH 7.5, 50 mM NaCl,
609 10% (v/v) glycerol) for two 2 h steps and one overnight step. For IslA used in
610 crystallography, the dialysis buffer was modified to not include glycerol (50 mM HEPES
611 pH 7.5, 50 mM NaCl). The dialyzed protein solution was concentrated via centrifugation
612 in a 20 mL 30 kDa centrifuge filter (IslA) or 6 mL 10kDa centrifuge filter (IslB) (3,220 g,
613 20 min spins) until the desired concentration was reached. Finally, all proteins were
614 aliquoted into cryovials fitted with an O-ring, flash frozen in liquid N_2, and stored at -80
615 ˚C. The cryovials with IslB were sealed in anoxic Hungate tubes (ChemGlass) before
616 freezing.
617
618 Recombinant enzymes used for enzymatic assays were handled in an anoxic vinyl
619 chamber (Coy Laboratories) (97% N_2/3% H_2 atmosphere). Samples were routinely
620 rendered anoxic as follows. Consumable goods were brought into the glovebox the day
621 before being used. Solid chemicals were brought into the anoxic chamber in Eppendorf
622 tubes that had been perforated. Protein solutions were either purified and stored under
623 anoxic conditions (IslB), or rendered anoxic before use by transfer to amber LC-MS

vials on ice that were sealed with septa and N_2 was passed over the headspace for 15 min before being brought into the anoxic chamber (IslA). Buffer components were routinely rendered anoxic by sparging them with N_2 prior to use.

Crystallization of IslA from B. wadsworthia

Initial screening was performed with the aid of an Art Robbins Phenix micro-pipetting robot and Formulatrix Rock Imager; initial crystallization conditions of a well solution containing 200 mM calcium acetate and 20% w/v PEG 3350 were found using the Hampton PEG/ION HT screen. Optimized crystals of glycerol-bound IslA from *Bilophila wadsworthia* were grown aerobically by hanging drop vapor diffusion at 22 ˚C. 1 μL of unactivated IslA protein with intact N-terminal His-tag (7.5 mg/mL in a buffer containing 50 mM HEPES pH 7.5, 50 mM NaCl, 10% (v/v) glycerol and 3 mM Isethionate was mixed with 1 μL of an optimized precipitant solution (200 mM calcium acetate and 15% w/v PEG 3350) in a sealed well with 500 μL of precipitant solution. Crystals grew after 2 weeks and were transferred in three steps of increasing glycerol concentration into a final cryogenic solution containing the precipitant solution supplemented with 20% (v/v) glycerol and flash frozen in liquid nitrogen.

Crystals of isethionate-bound IslA grew after 2 months, aerobically, by hanging drop vapor diffusion at 22 ˚C. 1 μL of unactivated IslA protein with intact N-terminal His-tag (7.5 mg/mL in a buffer containing 50 mM HEPES pH 7.5, 50 mM NaCl, and 30 mM sodium isethionate) was mixed with 1 μL of precipitant solution (0.16 M NaBr and 20%

PEG 3350) in a sealed well with 500 μL of precipitant solution. Crystals were cryoprotected with paraffin oil and flash frozen in liquid nitrogen.

Data Collection and Structure Determination of IslA

A native dataset of IslA was collected at the Advanced Photon Source (Argonne, IL) on beamline 24ID-C using the Pilatus-6M pixel array detector at a temperature of 100 K and wavelength of 0.9792 Å (12662 eV). Data were indexed, integrated and scaled in HKL2000 (Otwinowski and Minor, 1997) in the space group $P2_12_12$ to 2.26 Å resolution (see Table 1, below).

The structure of IslA was solved by molecular replacement in Phaser (Mccoy et al., 2007) using chain A of the structure of CutC from *Desulfovibrio alaskensis* (PDB 5FAU, 34.4% identity) (Bodea et al., 2016) after trimming side chains non-identical to IslA with Sculptor (Bunkoczi and Read, 2011). A solution with two IslA monomers, each forming a physiological dimer by crystallographic symmetry, were found (LLG and TFZ scores of 229.343 and 16.2, respectively), in the asymmetric unit (ASU). An initial round of automated model building and structure refinement was performed using Phenix AutoBuild (Terwilliger et al., 2008) (yielding R_{work} and R_{free} of 29.52% and 33.94%, respectively). After a rigid body refinement of the automated model, the model was extensively rebuilt using iterative steps of manual model building in Coot (Emsley and Cowtan, 2004) and refinement in Phenix (Adams et al., 2010) using atomic coordinates, atomic displacement parameters (B-factors) and two-fold non-crystallographic symmetry

(NCS) restraints, without sigma cutoffs. Water molecules were added and verified manually in later stages of refinement using Fo-Fc electron density map contoured to 3.0σ as criteria. NCS restraints were released in final stages of refinement. Refinement statistics can be found in Table 1.

The final structure of IslA contains 2 chains each with 6-830 (of 830 residues) and a glycerol molecule in the active site. Composite omit maps calculated in Phenix (Adams et al., 2010) were used to validate the model. Model geometry was analyzed using MolProbity (Chen et al., 2010). Ramachandran statistics analyzed by MolProbity (Chen et al., 2010) indicated 97.3%, 2.6%, and 0.1% of residues in the favored, allowed, and disallowed regions, respectively, and 98.7% of residues have favorable rotamers. Ile469 of chain A and B were the only two Ramachandran outliers, but best fit the composite omit density. PyMol was used to generate figures (Schrodinger, 2010). Crystallography software packages were compiled by SBGrid. (Morin et al., 2013)

Data Collection and Structure Determination of Ise-bound IslA

A substrate-bound dataset of IslA was collected at the Advanced Photon Source (Argonne, IL) on beamline 24ID-E using the Pilatus-6M pixel array detector at a temperature of 100 K and wavelength of 0.9792 Å (12662 eV). Data were indexed, integrated and scaled in HKL2000 (Otwinowski and Minor, 1997) in the space group $P2_12_12_1$ to 2.70 Å resolution (see Table 1, below).

690 The structure of IslA was solved by molecular replacement in Phaser (Mccoy et al.,
691 2007) using chain A of the structure of IslA with glycerol bound after removal of ligands
692 and water molecules. A solution with four IslA monomers, forming a dimer of dimers,
693 were found (LLG and TFZ scores of 14148.983 and 121.0, respectively), in the
694 asymmetric unit (ASU). After a rigid body refinement of the automated model, the model
695 was extensively rebuilt using iterative steps of manual model building in Coot (Emsley
696 and Cowtan, 2004) and refinement in Phenix (Adams et al., 2010) using atomic
697 coordinates, atomic displacement parameters (B-factors) and two-fold non-
698 crystallographic symmetry (NCS) restraints, without sigma cutoffs. The isethionate
699 ligand parameter files were generated using the eLBOW tool of Phenix (Moriarty et al.,
700 2009), and correct ligand placement was verified using composite omit maps. Water
701 molecules were added and verified manually in later stages of refinement using Fo-Fc
702 electron density map contoured to 3.0σ as criteria. Refinement statistics can be found in
703 Table 1.
704
705 The final structure of isethionate-bound IslA contains 4 chains each with 6-830 (of 830
706 residues) and an isethionate molecule in each active site. Composite omit maps
707 calculated in Phenix (Adams et al., 2010) were used to validate the model. Model
708 geometry was analyzed using MolProbity (Chen et al., 2010). Ramachandran statistics
709 analyzed by MolProbity (Chen et al., 2010) indicated 96.9%, 2.9%, and 0.2% of
710 residues in the favored, allowed, and disallowed regions, respectively, and 99.1% of
711 residues have favorable rotamers. Ile469 of chain A, B, C and D as well as Thr313 of

712 chain B were the only Ramachandran outliers, but best fit the composite omit density.
713 PyMol was used to generate figures (Schrodinger, 2010). Crystallography software
714 packages were compiled by SBGrid (Morin et al., 2013).
715
716 *Generation of Glycyl Radical in IslA*
717 The GRE was activated as described previously (Peck et al., 2019) in an anoxic
718 chamber by incubating IslB (80 µM), IslA (40 µM), acriflavine (100 µM), *S*-
719 adenosylmethionine (1 mM), and bicine (50 mM pH 7.5) in reaction buffer (50 mM
720 HEPES pH 7.5, 50 mM NaCl) at 25 ˚C for 2 h in a 275 µL scale for EPR spectroscopy.
721 The entire activation mixture was then loaded EPR tubes with 4 mm outer diameter and
722 8" length (Wilmad LabGlass), sealed, removed from the anoxic chamber, and slowly
723 frozen in liquid N_2. Perpendicular mode X-band EPR spectra were recorded on either a
724 Bruker ElexSysE500 EPR instrument equipped with a quartz finger dewar (Wilmad Lab-
725 Glass) for acquiring spectra at 77 K with liquid N_2 or a Bruker EMX-Plus EPR instrument
726 equipped with a Bruker/ColdEdge 4K waveguide cryogen-free cryostat set at 77K. The
727 samples were acquired with the following parameters on the ElexSysE500 EPR:
728 microwave frequency: 9.45 GHz; power: 20 µW (40 dB attenuation); center field: 3350
729 Gauss; sweep width: 200 Gauss; conversion time: 20.48 ms; modulation gain: 60 dB
730 modulation gain for samples; 30 dB for external standards; time constant: 20.48 ms;
731 modulation amplitude: 4 G; modulation frequency: 100 kHz. The samples were acquired
732 with the following parameters on the EMX-Plus EPR: microwave frequency: 9.45 GHz;
733 power: 1.262 µW (52 dB attenuation); center field: 3350 Gauss; sweep width: 200

734 Gauss; conversion time: 41.97 ms; modulation gain: 30 dB; time constant: 0.01 ms;
735 modulation amplitude: 4 G; modulation frequency: 100 kHz. Normalization due to
736 differences in modulation gain were automatically performed by the spectrometer.
737 Typically, only a single scan was recorded on the ElexSysE500 to minimize any
738 disruption due to bubbling from the liquid N_2, whereas typically 5 scans were recorded
739 on the EMX-Plus. The field was calibrated by using an external standard of
740 bisdiphenylene-β-phenylallyl (BDPA) with g = 2.0026 (Bruker). An external standard of
741 Frémy salt was prepared by dissolving $K_2(SO_3)_2NO$ in either anoxic 0.5 M $KHCO_3$ or
742 anoxic 20 mM HEPES pH 7.2. The concentration of the standard measured by its
743 absorbance at 248 nm (ε = 1,690 M^{-1} cm^{-1}) using a NanoDrop 2000 UV-Vis
744 Spectrophotometer. The double integral of the Frémy salt standard was calculated on
745 the EPR spectrometer and then used to determine the concentrations of each of the
746 protein samples from that set of EPR measurements. Frémy salt standards were
747 prepared fresh and run for each set of EPR measurements on either instrument. The
748 EPR spectra from the activation mixtures were simulated using EasySpin in MatLab
749 using the Levenberg/Marquardt algorithm (Stoll and Schweiger, 2006).
750
751 *Detection of Sulfite for Endpoint Assays*
752 IslA was first activated as described above for EPR spectroscopy on a 50 µL or 100 µL
753 scale. Activated IslA (5.9 µM total GRE) was then added to reaction buffer (50 mM
754 HEPES pH 7.5, 50 mM NaCl) supplemented with yeast alcohol dehydrogenase (8 µM)
755 and NADH (3 mM) in a 50 µL scale, and the reaction initiated by addition of 10 mM

isethionate. The reaction mixture incubated for 1 h and was then transferred out of the anoxic chamber and derivatized according to a previously reported procedure (Peck et al., 2019). To distinguish catalytically dead mutants from mutants with minimal activity toward isethionate, a 2 h incubation with 10 mM isethionate and 11.8 μM total IslA was also performed. The reactions were repeated in quadruplicate. For derivatization, a 100 mL solution of 0.3 M boric acid, 0.3 M KCl, and 0.02 M Na_2-EDTA was mixed with a 50 mL solution of 0.3 M Na_2CO_3 and 0.02 M Na_2-EDTA to adjust the solution of the mixture to pH 8.8. 150 μL of this solution was added to each reaction, followed by 50 μL of an acetone solution containing N-(9-acridinyl)maleimide (0.1% w/v). Freshly prepared sodium sulfite standards were derivatized at the same time. The reactions were incubated at 37 ˚C for 2 h in the dark. The fluorescence intensity was recorded using a Synergy HTX Plate Reader (BioTek) with the excitation wavelength was 360 nm and the emission wavelength was 440 nm.

Kinetics Analysis of Isethionate Cleavage

IslA was first activated as described above for EPR spectroscopy on a 250 μL scale. Activated IslA (0.8-4.5 μM total IslA depending on mutant activity) was mixed with yeast alcohol dehydrogenase (2 μM) and NADH (200 μM) on a 200 μL scale in a 96-well plate, as described previously (Peck et al., 2019). The reactions were initiated by addition of isethionate (1-50 mM), and the plate was loaded into a PowerWave HT plate reader (BioTek) set to 30 ˚C. The pathlength-corrected absorbance at 340 nm was recorded every 10 s for up to 30 min. The observed rate constant was fit to the standard

Michaelis-Menten steady-state equation ($k_{obs} = k_{cat}$* [S]/(K_M + [S])) in Graphpad Prism 8.0.1.

Synthesis of 2,2-d_2-isethionate

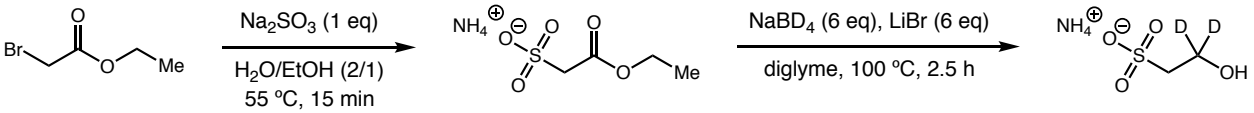

The deuterated substrate was prepared using a previously reported procedure (Harmer et al., 2005).

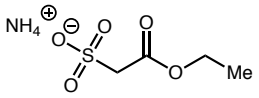

Ammonium ethyl sulfoacetate. Under air, a 50-mL round-bottom flask (rbf) was equipped with a magnetic stir bar, then charged with sodium sulfite (2.5 g, 20 mmol, 1 equiv.) and distilled water (8 mL). The mixture was sonicated to yield a clear solution then it was cooled to 0 ºC with stirring. A solution of ethyl bromoacetate (2.2 mL, 3.3 g, 20 mmol) in absolute ethanol (4 mL) was added over 5 minutes. Precipitate formed heavily by the end of the addition process. The mixture was heated to 55 ºC for 15 minutes. Most precipitate dissolved during the heating period. While hot, the mixture was decanted to remove residual precipitate. The clear solution was cooled then concentrated to yield a waxy solid.

The resulting solid was suspended in a hot solution of AcOH/EtOAc (2/1 ratio, 18 mL, ~ 60 ºC). The mixture was swirled at 60 ºC for about 10 minutes, then it was quickly filtered over Celite. Once the solution was cooled to room temperature, EtOAc (50 mL)

was added, which resulted in a white precipitate. The precipitate was separated by centrifugation. The solid was resuspended in EtOAc and separated again by centrifugation. This washing procedure was repeated two more times. The precipitate was dissolved in distilled water (3 mL). The pH of the solution was approximately 3. Amberlite IR120 resin (Oakwood) was slowly added to adjust to the pH to 1. The mixture was decanted to remove the resin. The resulting solution was cooled on an ice bath, then cooled concentrated ammonium hydroxide was added to adjust the pH to 7. The final solution was concentrated by lyophilization to yield an off-white solid.

The off-white solid was dissolved in ethanol (2 mL), then it was filtered with a syringe filter. Diethyl ether (20 mL) was slowly added, which resulted in a white precipitate. The solid was isolated via filtration and dried under hi-vac overnight. NMR data is in agreement with previously reported data. According to the literature, ~35% by weight of the crude solid is ammonium ethyl sulfoacetate. Since the next step utilizes excess reagents (>10 equiv.), we assumed a 35% by weight for stoichiometry calculation. The procedure yielded 1.5 g product (35% w/w, 14% yield).

^{1}H NMR (D_2O, 400 MHz): δ 1.31 (t, J = 7.1z Hz, 3H), 3.98 (s, 2H), 4.27 (q, J = 7.2 Hz, 2H).

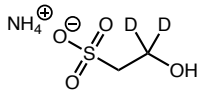

Ammonium [2,2-$^2H_2$]-2-Hydroxyethanesulfonate. Under nitrogen, a two-neck 100-mL rbf, equipped with a reflux condenser and a magnetic stir bar, was charged with sodium

borodeuteride (1.1 g, 26 mmol, 13 equiv.) and diglyme (10 mL). The mixture was stirred for 15 minutes at room temperature before lithium bromide (2.3g, 26 mmol, 13 equiv.) was added. This mixture was stirred for another 30 minutes at room temperature. Ammonium ethyl sulfoacetate (35% by weight, 1.1 g, 2.0 mmol) was added then the mixture was heated at 100 ºC for 2.5 hours under nitrogen.

The mixture was cooled to room temperature then quenched by slow addition of MeOH (~ 20 mL total) and distilled water (~ 20 mL). MeOH and water were added dropwise to limit gas evolution during the quenching process. The pH of the final solution was about 11. Amberlite IR120 resin (Oakwood) was added to adjust the pH to 1. This resulted in a yellow solution. The resin was removed by decanting, then 50 mL of MeOH was added before the solution was concentrated to yield an oily mixture. This mixture was resuspended in 50 mL of MeOH and the mixture was concentrated. This process was repeated 5 more times, which resulted in a sticky solid. The solid was dissolved in water (2 mL) and cooled on an ice bath. Cooled concentrated ammonium hydroxide was added to adjust the pH to 7. The final solution was concentrated by lyophilization to yield a light brown solid.

The light brown solid was dissolved in 5 mL of methanol, then the mixture was filtered with a syringe filter. Diethyl ether (about 30 mL) was added, which resulted in a white precipitate. The precipitate was isolated by filtration, then dried on hi-vacuum overnight.

The product was further purified by dissolving in water (1 mL), and then ethanol (4 mL) was added. The mixture was allowed to sit at 4 ºC overnight. The precipitate was filtered then the solution was concentrated to yield the final product as a white solid (110 mg, 37% yield). NMR data is in agreement with previously reported data.

^{1}H NMR (D_2O, 400 MHz): δ 3.18 (s, 2H).

Detection of deuterium-labeled ethanol

IslA was first activated on a 250 µL scale as described above for EPR spectroscopy. After the 2 h incubation, a boiled enzyme control was prepared by incubating the activation mixture at 95 ºC for 10 minutes in a C1000 Gradient Cycler (Bio-Rad). Either active IslA or boiled IslA (1.6 µM total IslA) was mixed with NADH (3 mM), yeast alcohol dehydrogenase (8 µM) and either unlabeled or 2,2-d_2-isethionate (2 mM) in reaction buffer (50 mM HEPES pH 7.5, 50 mM NaCl) on an 800 µL scale. The reactions were set up in triplicate. The reaction mixtures were left in the anoxic chamber overnight. After overnight incubation, they were removed from the chamber and immediately added to a 10 mL headspace vial with 4.2 mL of water and 1.7 g NaCl and sealed tightly. Vials were stored at 4 ºC prior to GC-MS analysis.

Headspace gas chromatography-mass spectrometry (GC-MS) experiments were conducted on the TRACE 1310 Gas Chromatograph with a Q Exactive GC Orbitrap. Headspace extractions were performed at 85 ºC with agitation for 10 minutes on an autosampler (Thermo Scientific TriPlus RSH). A transfer syringe held at 120 ºC was used to inject 1 mL of headspace sample into the instrument. The column used was a

fused-silica capillary column of cross-linked DB-624UI (30 m × 0.32 mm × 1.80 µm, Agilent). The inlet helium carrier gas flow rate was 2.3 mL/min. For spectra collected with positive chemical ionization (PCI), the conditions were as follows: split ratio of 20; oven temperature program 30 ºC for 3 min, 50 ºC/min to 250 ºC, hold for 3 min; MS transfer line at 220 ºC; CI gas type methane with 2 mL/min flow rate; ion source temperature 120 ºC; full MS-SIM from 1 – 7 min in positive polarity; resolution 120,000; AGC target 1e6; scan range 30 – 100 m/z; max IT auto. For spectra collected with electron impact (EI) ionization the conditions were: split ratio of 20; oven temperature program 30 ºC for 3 min, 50 ºC/min to 250 ºC, hold for 3 min; MS transfer line at 220 ºC; ion source temperature 200 ºC; full MS-SIM from 1 – 7 min in positive polarity; resolution 120,000; AGC target 1e6; scan range 30 – 100 m/z; max IT auto. The retention time of the ethanol peak was 2.03-2.07 min. The entire peak was extracted with background correction to generate the displayed mass spectra. The relative intensity is scaled to the maximum intensity in the plotted range of m/z values. Data was analyzed using Thermo Xcalibur Qual Browser 3.0.63.

High-level model QM calculations

Electronic structure calculations were performed to investigate the energetics of representative models of the isethionate H abstraction by cysteine radical. The cysteine radical was modeled as $CH_3S\bullet$ and the Glu470 side chain, where present, was modeled as acetate. Fully optimized structures of the reactant substrates and transition states (TSes) were obtained using ORCA (CITE) v.4.0.1.2. Free gas-phase geometry

optimizations of substrates and TSes were performed using hybrid (B3LYP (CITE)) density functional theory (DFT) with the 6-31G* basis set (CITE). Frequency calculations were performed on the optimized geometries at the same level of theory, i.e., B3LYP/6-31G*, and thermodynamic corrections were obtained.

The geometry optimizations of substrates and TSes were carried out in redundant internal coordinates using the BFGS and Bofill algorithms, respectively, with default thresholds of 3×10^{-4} hartree/bohr for the maximum gradient and 5×10^{-6} hartree for SCF convergence. Initial structures of intermediates were built by hand in Avogadro (CITE) v1.20, and TSes were modified from the optimized intermediates by stretching the forming and breaking bonds. All initial and optimized geometries are provided in the Supporting Information .zip file.

Numerical Hessian calculations were carried out where the Hessian was computed using the central differences approach after 6*N* displacements (where *N* is the number of atoms in a given system). The presence of a single imaginary frequency was confirmed for both the TSes corresponding to the hydrogen atom transfer from isethionate to $CH_3S\bullet$ in the presence and absence of acetate, while the substrates had no imaginary frequencies indicating that the converged geometries of substrates corresponded to energy minima.

Thermochemistry properties (i.e., energy, *U*, enthalpy, *H*), entropy, *S*, and the Gibbs free energy, *G*) were then computed at 298.15 K and 1 atm for these gas-phase models using statistical mechanics (Table S1). Single point energy calculations were carried out on the optimized geometries at the domain-localized pair natural orbital coupled cluster single doubles and perturbative triples (DLPNO-CCSD(T) (CITE)) level of theory using tight PNO thresholds (Table S2). Dunning-style correlation consistent double-ζ and triple-ζ (i.e., aug-cc-pVDZ and aug-cc-pVTZ) basis sets were employed to enable two-point extrapolation (CITE) to the complete basis set (CBS) limit. Since implicit solvent models are not implemented in DLPNO-CCSD(T), the gas phase DLPNO-CCSD(T) energies were corrected with the conductor-like polarizable continuum model (CITE) (C-PCM) solvation energies in combination with the conductor-like screening solvent model (COSMO) epsilon function type obtained at the MP2/CBS level of theory in ORCA (Table S2). The solvent corrections were computed as the difference between gas-phase MP2/CBS single point energies and solvent-corrected MP2/CBS single point energies. The solvent corrections were carried out with two dielectric values, $\varepsilon = 10$ and 78.39, approximately mimicking the protein and an aqueous environment, respectively (Table S3). The solvent-corrected DLPNO-CCSD(T)/CBS energies were used in combination with the thermodynamic corrections to predict the value of G^0 at a temperature of 298.15 K and pressure of 1 atm. The final reported results in the main text are for the free energy of activation with $\varepsilon = 10$ modeling the environment applied to the DLPNO-CCSD(T)/CBS energies.

QUANTIFICATION AND STATISTICAL ANALYSIS

Statistical analysis was performed using either GraphPad Prism or Microsoft Excel. Statistical details of the experiments can be found in the corresponding figure legends.

Supplemental Titles and Tables

Fig. S1, related to Figure 1: GRE reaction schemes. Eliminated functional groups and bond that undergoes cleavage are shown in blue. Moieties undergoing oxidation to drive elimination are shown in red.

Fig. S2, related to Figure 2: Comparison of the glycerol-bound and Ise-bound IslA structures. (A) $2F_o$-F_c composite omit map contoured to 1.5 σ around glycerol. IslA is shown in orange with Gly loop and Cys loop shown in yellow and purple, respectively. Water molecules are shown as red spheres. (B) Isethionate-bound structure with $2F_o$-F_c composite omit map contoured to 1.5σ (blue) and with F_o-F_c map contoured to +3σ (bright green) or to -3σ (red). (C) Glycerol and a water molecule refined into active site density of isethionate-bound structure with $2F_o$-F_c composite omit map contoured to 1.5σ and with F_o-F_c map contoured to +3σ (bright green) or to -3σ (red). (D) Overlay of glycerol-bound IslA (orange) and isethionate-bound IslA (green). (E) A different orientation of the Ise-bound IslA structure and maps shown in panel B. In this refined orientation of Ise (green carbons), it is the *pro*-R hydrogen on C2 that points toward Cys468. (F) When Ise (red carbons) is modeled into the map shown in panel B such that the *pro*-S hydrogen on C2 is pointing toward Cys468, the fit to the density is less good. Panel E and F additionally show composite omit map contoured to 1.5σ (blue) for the side chains of residues that surround the substrate. Chain A was used to generate panels F and E. Chain D was used for all other structure figures.

Fig. S3, related to Figure 3: A Multiple sequence alignment for key structural regions for putative IslAs and several characterized GREs. NCBI Accession codes are listed for each sequence, numbered as residues in IslA from *B. wadsworthia* (WP_009733371.1). Residues conserved in all GREs are show in yellow. Residues conserved in GRE eliminases are shown in orange. Residues conserved in IslAs are shown in green. Sequences were aligned using Clustal Omega (Sievers et al., 2011).

Fig. S4, related to Figure 5: Channel views and conservation in GREs. (A) Van der Waals surface of BSS (PDB ID: 5BWE) is shown as a cutaway with substrates fumarate and toluene (red) above the glycyl radical domain (yellow) and Cys loop (purple). The channel contains a bottle neck created by the residues shown in green and is capped by BSS-β (blue) (B) The substrate channel (pink) of BSS between the surface of the protein and fumarate-binding site as generated by CAVER 3.0 (Chovancova et al.,

2012) using the BSS-αβγ structure with BSS-β removed. (C) Conservation of residues of substrate channel (transparent surface) of BSS α subunit (PDB ID: 4PKC). Residues within 4 Å of the putative substrate channel are shown as sticks and colored by conservation score as computed by ConSurf (Ashkenazy et al., 2016) with a gradient from lower scores (more conserved) show in green to higher scores (less conserved) shown in red. (D-F) As C, but for (D) HPAD α subunit (PDB ID: 2Y8N), (E) glycerol-bound IslA, and (F) HypD (PDB ID: 6VXE).

Fig. S5, related to Table 2: SDS-PAGE of recombinant enzymes purified for this study and sulfite endpoint detection demonstrates IslA variant activity toward isethionate. (A) Precision Plus Protein All Blue Standards (BioRad), IslA-WT (lane 1), and IslB (lane 2). (B) Precision Plus Protein All Blue Standards (BioRad), IslA-WT (lane 1), IslA-R189E (lane 2), IslA-R189E/R678E (lane 3), IslA-I192A (lane 4), IslA-Q193A (lane 5), IslA-W374F (lane 6), IslA-W374Y (lane 7), IslA-C468S (lane 8), IslA-E470Q (lane 9), IslA-R678E (lane 10), IslA-V680A (lane 11), IslA-F682A (lane 12), IslA-F682Y (lane 13), IslA-G805A (lane 14). (C) Initial assay conditions with a 1-hour incubation of activated GRE with isethionate demonstrated sulfite production for WT, W374F, W374Y and I192A. (D) A 2-hour incubation with twice the enzyme concentration shows that F682A and F682Y are also capable of generating sulfite from isethionate. All assays were repeated in quadruplicate. Bars represent the mean ± standard deviation of the replicates.

Fig. S6, related to Figure 6: Sulfonates. (A) Sulfonate molecules that are either absent in the PDB or bound in a nonphysiological mode and (B-G) physiological sulfonate binding modes of isethionate, sulfolactate, and taurine as either substrates or products.

Fig. S7, related to Figure 6: The IslA and CutC active sites appear primed for elimination chemistry, in contrast to the proposed migration chemistry of EAL. Hydrogen bond interactions and CH—O bond interactions are show in black and yellow dashes, respectively. (A) The IslA active site with Ise and nearby residues shown as sticks. (B) Another view of IslA with van der Waals spheres shown for Q193, T312, and Ise. (C) The CutC active site with choline and nearby residues shown as sticks. (D) Another view of CutC with van der Waals spheres shown for T502, E491, and choline. (E) Simplified reaction scheme for EAL (Mori et al., 2014; Toraya, 2003). (F) The EAL active site with ethanolamine and nearby residues shown as sticks (PDB ID 3ABO) (Shibata et al., 2010). (G) Another view of EAL with van der Waals spheres shown for M392, Q162, N193, and ethanolamine.

System	ZPE (kcal/mol)	ZPE + thermal energy (U-E_{el}) (kcal/mol)	Entropy (TS) (kcal/mol)	G-E_{el} (H-TS-E_{el} = U+k_BT-TS-E_{el} = ZPE + thermal + k_BT - TS) (kcal/mol)
acetate	30.32	33.07	20.13	13.53
CH_3S	23.02	24.94	17.73	7.80
isethionate	52.66	57.42	25.57	32.44
isethionate-acetate	84.56	92.84	34.21	59.22
isethionate-CH_3S (TS)	72.61	79.91	32.23	48.27
isethionate-CH_3S-acetate (TS)	104.78	115.48	40.07	76.00

Table S1: Thermodynamic corrections to the electronic energy (E_{el}) in kcal/mol obtained with B3LYP/6-31G*-optimized geometries of acetate, $CH_3S^{\cdot}$, isethionate, isethionate-acetate complex, and the transitions states (TSes) corresponding to hydrogen atom transfer from isethionate to $CH_3S^{\cdot}$, both in the presence and absence of acetate. Zero point energy (ZPE) (column 2), ZPE and thermal energy (column 3), entropy multiplied by temperature (TS, where T=298.15 K; column 4), and the energy that is to be added to E_{el} to transform it into G^0 (G-E_{el}; column 5) in kcal/mol are shown. Inner energy, U=ZPE + thermal energy + E_{el}. G-E_{el}=ZPE + thermal energy + k_BT - TS, where k_B is the Boltzmann constant and T=298.15K.

System	DLPNO-CCSD(T)/CBS (kcal/mol)	DLPNO-CCSD(T)/CBS + solv. corr. with ε=10 (kcal/mol)	DLPNO-CCSD(T)/CBS + solv. corr. with ε=78.39 (kcal/mol))	DLPNO-CCSD(T)/CBS + solv. corr. with ε=10 + G - E_{el} (kcal/mol)	DLPNO-CCSD(T)/CBS + solv. corr. with ε=78.39 + G - E_{el} (kcal/mol
acetate	-143261.94	-143321.66	-143330.71	-143308.13	-143317.18
CH_3S	-274585.59	-274587.59	-274587.93	-274579.79	-274580.13
isethionate	-487969.01	-488026.40	-488035.18	-487993.96	-488002.74
isethionate-acetate	-631203.22	-631350.92	-631372.76	-631291.70	-631313.54
isethionate-CH_3S (TS)	-762542.57	-762599.13	-762608.08	-762550.86	-762559.81
isethionate-CH_3S-acetate (TS)	-905786.31	-905928.36	-905949.56	-905852.36	-905873.56

Table S2: Relative gas-phase DLPNO-CCSD(T)/CBS electronic energies (column 2), solvent corrected DLPNO-CCSD(T)/CBS energies with solvent correction energies

obtained at the MP2/CBS level of theory for dielectric values of 10 (column 3) and 78.39 (column 4), Gibbs free energies at T=298.15 K and 1 atm pressure for dielectric values of 10 (column 5) and 78.39 (column 6) are shown. All energies reported here are in units of kcal/mol. The two-point extrapolation formula based on the aug-cc-pVDZ and aug-cc-pVTZ energies is used to extrapolate to the complete basis set limit (CITE) for DLPNO-CCSD(T). DLPNO-CCSD(T)/CBS energies were computed using tight PNO thresholds, which refer to the default thresholds of TCutPairs = 10^{-5}, TCutPNO = 1.00 x 10^{-7}, and TCutMKN = 10^{-3}.

System	**Activation energy: DLPNO-CCSD(T)/CBS + solv. corr. with ε=10 (kcal/mol)**	**Activation energy: DLPNO-CCSD(T)/CBS + solv. corr. with ε=78.39 (kcal/mol))**	**Activation energy: DLPNO-CCSD(T)/CBS + solv. corr. with ε=10 + G - E_{el} (kcal/mol)**	**Activation energy: DLPNO-CCSD(T)/CBS + solv. corr. with ε=78.39 + G - E_{el} (kcal/mol**
isethionate-CH_3S (TS)	14.86	15.04	22.89	23.07
isethionate-CH_3S-acetate (TS)	10.15	11.14	19.13	20.12

Table S3: Activation energies of TSes corresponding to hydrogen atom transfer from isethionate to CH_3S in the presence (row 3) and absence (row 2) of acetate. Activation energies incorporating MP2/CBS solvent corrections to the gas-phase DLPNO-CCSD(T)/CBS electronic energies for dielectric values of 10 (column 2) and 78.39 (column 3) and activation energies obtained from Gibbs free energies of systems for dielectric values of 10 (column 4) and 78.39 (column 5) are shown. All the reported energies are in kcal/mol.

Oligonucleotide	**Target**	**Sequence (5′ to 3′)**
Bwad_IslA_R189E_F	IslA-R189E	gcacccactggatggaggactcgaaagaggaggtttcgttg
Bwad_IslA_R189E_R	IslA-R189E	caacgaaacctcctctttcgagtcctccatccagtgggtgc
Bwad_IslA_I192A_F	IslA-I192A	gtcatgcacccactgggcggaggaacggaaagag
Bwad_IslA_I192A_R	IslA-I192A	ctctttccgttcctccgcccagtgggtgcatgac
Bwad_IslA_Q193A_F	IslA-Q193A	cctccatcgcgtgggtgcatg
Bwad_IslA_Q193A_R	IslA-Q193A	catgcacccacgcgatggagg
Bwad_IslA_W374F_F	IslA-W374F	ccaatggtgacggcttcgaagtgagcgtaaccttcg
Bwad_IslA_W374F_R	IslA-W374F	cgaaggttacgctcacttcgaagccgtcaccattgg
Bwad_IslA_W374Y_F	IslA-W374Y	ccaatggtgacggcttcatagtgagcgtaaccttcg
Bwad_IslA_W374Y_F	IslA-W374Y	cgaaggttacgctcactatgaagccgtcaccattgg
Bwad_IslA_C468S_F	IslA-C468S	gtgtccggcagcatcgaaatc

Bwad_IslA_C468S_R	IslA-C468S	gatttcgatgctgccggacac
Bwad_IslA_E470Q_F	IslA-E470Q	ggctgcatccaaatccgtatg
Bwad_IslA_E470Q_R	IslA-E470Q	catacggatttggatgcagcc
Bwad_IslA_R678E_F	IslA-R678E	gaggtgaagggcacgtactcggcgtcgttgttgatgc
Bwad_IslA_R678E_R	IslA-R678E	gcatcaacaacgacgccgagtacgtgcccttcacctc
Bwad_IslA_F682A_F	IslA-F682A	acgtgagaggtggcgggcacgtaacg
Bwad_IslA_F682A_R	IslA-F682A	cgttacgtgcccgccacctctcacgt
Bwad_IslA_F682Y_F	IslA-F682Y	gcacgtgagaggtatagggcacgtaacgggc
Bwad_IslA_F682Y_R	IslA-F682Y	gcccgttacgtgccctatacctctcacgtgc
Bwad_IslA_G805A_F	IslA-G805A	cgcatcgccgcgtacagcgcc
Bwad_IslA_G805A_R	IslA-G805A	ggcgctgtacgcggcgatgcg

Table S4: Oligonucleotides used for cloning.

References

Adams, P.D., Afonine, P.V., Bunkóczi, G., Chen, V.B., Davis, I.W., Echols, N., Headd, J.J., Hung, L.W., Kapral, G.J., Grosse-Kunstleve, R.W*., et al.* (2010). PHENIX: A comprehensive Python-based system for macromolecular structure solution. Acta Crystallogr. D Biol. Crystallogr. *66*, 213-221.

Ashkenazy, H., Abadi, S., Martz, E., Chay, O., Mayrose, I., Pupko, T., and Ben-Tal, N. (2016). ConSurf 2016: an improved methodology to estimate and visualize evolutionary conservation in macromolecules. Nucleic Acids Res. *44*, W344-350.

Backman, L.R., Huang, Y.Y., Andorfer, M.C., Gold, B., Raines, R.T., Balskus, E.P., and Drennan, C.L. (2020). Molecular basis for catabolism of the abundant metabolite trans-4-hydroxy-L-proline by a microbial glycyl radical enzyme. Elife *9*.

Backman, L.R.F., Funk, M.A., Dawson, C.D., and Drennan, C.L. (2017). New tricks for the glycyl radical enzyme family. Crit. Rev. Biochem. Mol. Biol. *52*, 674-695.

Baron, E.J., Curren, M., Henderson, G., Jousimies-Somer, H., Lee, K., Lechowitz, K., Strong, C.A., Summanen, P., Tuner, K., and Finegold, S.M. (1992). Bilophila wadsworthia isolates from clinical specimens. J. Clin. Microbiol. *30*, 1882-1884.

Baron, E.J., Summanen, P., Downes, J., Roberts, M.C., Wexler, H., and Finegold, S.M. (1989). Bilophila wadsworthia, gen. nov. and sp. nov., a unique gram-negative anaerobic rod recovered from appendicitis specimens and human faeces. J. Gen. Micro. *135*, 3405-3411.

Bodea, S., Funk, M.A., Balskus, E.P., and Drennan, C.L. (2016). Molecular Basis of C–N Bond Cleavage by the Glycyl Radical Enzyme Choline Trimethylamine-Lyase. Cell. Chem. Bio. *23*, 1206-1216.

1068 Bunkoczi, G., and Read, R.J. (2011). Improvement of molecular-replacement models with
1069 Sculptor. Acta Crystallogr. D Biol. Crystallogr. *67*, 303-312.

1070 Carbonero, F., Benefiel, A.C., Alizadeh-Ghamsari, A.H., and Gaskins, H.R. (2012). Microbial
1071 pathways in colonic sulfur metabolism and links with health and disease. Front. Physiol. *3*, 448.

1072 Chen, V.B., Arendall, W.B., Headd, J.J., Keedy, D.A., Immormino, R.M., Kapral, G.J., Murray,
1073 L.W., Richardson, J.S., and Richardson, D.C. (2010). MolProbity: all-atom structure validation for
1074 macromolecular crystallography. Acta Crystallogr. D Struct. Bio. *66*, 12-21.

1075 Chovancova, E., Pavelka, A., Benes, P., Strnad, O., Brezovsky, J., Kozlikova, B., Gora, A., Sustr, V.,
1076 Klvana, M., Medek, P*., et al.* (2012). CAVER 3.0: A Tool for the Analysis of Transport Pathways in
1077 Dynamic Protein Structures. PLoS Comp. Biol. *8*.

1078 Craciun, S., and Balskus, E.P. (2012). Microbial conversion of choline to trimethylamine requires
1079 a glycyl radical enzyme. Proc. Natl. Acad. Sci. *109*, 21307-21312.

1080 Craciun, S., Marks, J.A., and Balskus, E.P. (2014). Characterization of choline trimethylamine-
1081 lyase expands the chemistry of glycyl radical enzymes. ACS Chemical Biology *9*, 1408-1413.

1082 DiDonato, M., Krishna, S.S., Schwarzenbacher, R., McMullan, D., Agarwalla, S., Brittain, S.M.,
1083 Miller, M.D., Abdubek, P., Ambing, E., Axelrod, H.L*., et al.* (2006). Crystal structure of 2-
1084 phosphosulfolactate phosphatase (ComB) from Clostridium acetobutylicum at 2.6 A resolution
1085 reveals a new fold with a novel active site. Proteins *65*, 771-776.

1086 Emsley, P., and Cowtan, K. (2004). Coot: Model-building tools for molecular graphics. Acta
1087 Crystallogr. D Biol. Crystallogr. *60*, 2126-2132.

1088 Feliks, M., and Ullmann, G.M. (2012). Glycerol dehydratation by the B12-independent enzyme
1089 may not involve the migration of a hydroxyl group: a computational study. J. Phys. Chem. B *116*,
1090 7076-7087.

1091 Fellman, J.H., Roth, E.S., Avedovech, N.A., and McCarthy, K.D. (1980). The metabolism of
1092 taurine to isethionate. Arch. Biochem. Biophys. *204*, 560-567.

1093 Feng, Z., Long, W., Hao, B., Ding, D., Ma, X., Zhao, L., and Pang, X. (2017). A human stool-derived
1094 Bilophila wadsworthia strain caused systemic inflammation in specific-pathogen-free mice. Gut
1095 Pathogens *9*.

1096 Funk, M.A., Judd, E.T., Marsh, E.N.G., Elliott, S.J., and Drennan, C.L. (2014). Structures of
1097 benzylsuccinate synthase elucidate roles of accessory subunits in glycyl radical enzyme
1098 activation and activity. Proc. Natl. Acad. Sci. *111*, 10161-10166.

1099 Funk, M.A., Marsh, E.N.G., and Drennan, C.L. (2015). Substrate-bound structures of
1100 benzylsuccinate synthase reveal how toluene is activated in anaerobic hydrocarbon
1101 degradation. J. Biol. Chem. *290*, 22398-22408.

1102 Goldstein, E.J.C., Citron, D.M., Peraino, V.A., and Cross, S.A. (2003). Desulfovibrio desulfuricans
1103 bacteremia and review of human Desulfovibrio infections. J. Clin. Microbiol. *41*, 2752-2754.

1104 Ijssennagger, N., van der Meer, R., and van Mil, S.W.C. (2016). Sulfide as a Mucus Barrier-
1105 Breaker in Inflammatory Bowel Disease? Trends Mol. Med. *22*, 190-199.

1106 Kertesz, M.A. (2000). Riding the sulfur cycle - Metabolism of sulfonates and sulfate esters in
1107 Gram-negative bacteria. FEMS Microbiol. Rev. *24*, 135-175.

1108 Kovačević, B., Barić, D., Babić, D., Bilić, L., Hanževački, M., Sandala, G.M., Radom, L., and Smith,
1109 D.M. (2018). Computational Tale of Two Enzymes: Glycerol Dehydration with or Without B 12. J.
1110 Am. Chem. Soc. *140*, 8487-8496.

1111 LaMattina, J.W., Keul, N.D., Reitzer, P., Kapoor, S., Galzerani, F., Koch, D.J., Gouvea, I.E., and
1112 Lanzilotta, W.N. (2016a). 1,2-Propanediol dehydration in Roseburia inulinivorans: Structural
1113 basis for substrate and enantiomer selectivity. J. Biol. Chem. *291*, 15515-15526.

1114 LaMattina, J.W., Keul, N.D., Reitzer, P., Kapoor, S., Galzerani, F., Koch, D.J., Gouvea, I.E., and
1115 Lanzilotta, W.N. (2016b). 1,2-Propanediol Dehydration in Roseburia inulinivorans: STRUCTURAL
1116 BASIS FOR SUBSTRATE AND ENANTIOMER SELECTIVITY. J. Biol. Chem. *291*, 15515-15526.

1117 Laue, H., Denger, K., and Cook, A.M. (1997). Taurine reduction in anaerobic respiration of
1118 Bilophila wadsworthia RZATAU. Appl. Environ. Microbiol. *63*, 2016-2021.

1119 Levin, B.J., Huang, Y.Y., Peck, S.C., Wei, Y., Martínez-Del Campo, A., Marks, J.A., Franzosa, E.A.,
1120 Huttenhower, C., and Balskus, E.P. (2017). A prominent glycyl radical enzyme in human gut
1121 microbiomes metabolizes trans-4-hydroxy-L-proline. Science *355*.

1122 Lie, T.J., Godchaux, W., and Leadbetter, E.R. (1999). Sulfonates as terminal electron acceptors
1123 for growth of sulfite-reducing bacteria (Desulfitobacterium spp.) and sulfate- reducing bacteria:
1124 Effects of inhibitors of sulfidogenesis. Appl. Environ. Microbiol. *65*, 4611-4617.

1125 Lie, T.J., Pitta, T., Leadbetter, E.R., Godchaux Iii, W., and Leadbetter, J.R. (1996). Sulfonates:
1126 Novel electron accepters in anaerobic respiration. Arch. Microbiol. *166*, 204-210.

1127 Martins, B.M., Blaser, M., Feliks, M., Ullmann, G.M., Buckel, W., and Selmer, T. (2011).
1128 Structural basis for a Kolbe-type decarboxylation catalyzed by a glycyl radical enzyme. J. Am.
1129 Chem. Soc. *133*, 14666-14674.

1130 Mccoy, A.J., Grosse-Kunstleve, R.W., Adams, P.D., Winn, M.D., Storoni, L.C., and Read, R.J.
1131 (2007). Phaser crystallographic software. J. Appl. Cryst. *40*, 658-674.

1132 Mori, K., Oiwa, T., Kawaguchi, S., Kondo, K., Takahashi, Y., and Toraya, T. (2014). Catalytic roles
1133 of substrate-binding residues in coenzyme B12-dependent ethanolamine ammonia-lyase.
1134 Biochemistry *53*, 2661-2671.

Moriarty, N.W., Grosse-Kunstleve, R.W., and Adams, P.D. (2009). electronic Ligand Builder and Optimization Workbench (eLBOW): a tool for ligand coordinate and restraint generation. Acta Crystallogr. D Biol. Crystallogr. *65*, 1074-1080.

Morin, A., Eisenbraun, B., Key, J., Sanschagrin, P.C., Timony, M.A., Ottaviano, M., and Sliz, P. (2013). Collaboration gets the most out of software. Elife *2*, e01456.

Nishiyama, S., Takahashi, Y., Yamamoto, K., Suzuki, D., Itoh, Y., Sumita, K., Uchida, Y., Homma, M., Imada, K., and Kawagishi, I. (2016). Identification of a Vibrio cholerae chemoreceptor that senses taurine and amino acids as attractants. Sci. Rep. *6*, 20866.

O'Brien, J.R., Raynaud, C., Croux, C., Girbal, L., Soucaille, P., and Lanzilotta, W.N. (2004). Insight into the mechanism of the B12-independent glycerol dehydratase from *Clostridium butyricum*: preliminary biochemical and structural characterization. Biochemistry *43*, 4635-4645.

O'Brien, J.R., Schuller, D.J., Yang, V.S., Dillard, B.D., and Lanzilotta, W.N. (2003). Substrate-induced conformational changes in Escherichia coli taurine/alpha-ketoglutarate dioxygenase and insight into the oligomeric structure. Biochemistry *42*, 5547-5554.

Otwinowski, Z., and Minor, W. (1997). Processing of X-ray diffraction data collected in oscillation mode. Macromolecular Crystallography, Pt A *276*, 307-326.

Peck, S.C., Denger, K., Burrichter, A., Irwin, S.M., Balskus, E.P., and Schleheck, D. (2019). A glycyl radical enzyme enables hydrogen sulfide production by the human intestinal bacterium Bilophila wadsworthia. Proc. Natl. Acad. Sci. *116*, 3171-3176.

Rossocha, M., Schultz-Heienbrok, R., von Moeller, H., Coleman, J.P., and Saenger, W. (2005). Conjugated bile acid hydrolase is a tetrameric N-terminal thiol hydrolase with specific recognition of its cholyl but not of its tauryl product. Biochemistry *44*, 5739-5748.

Schrodinger, L. (2010). The PyMOL molecular graphics system. Version *1*, 0.

Shatalin, K., Shatalina, E., Mironov, A., and Nudler, E. (2011). H2S: A universal defense against antibiotics in bacteria. Science *334*, 986-990.

Shen, X., Carlström, M., Borniquel, S., Jädert, C., Kevil, C.G., and Lundberg, J.O. (2013). Microbial regulation of host hydrogen sulfide bioavailability and metabolism. Free Radical Biol. Med. *60*, 195-200.

Shibata, N., Tamagaki, H., Hieda, N., Akita, K., Komori, H., Shomura, Y., Terawaki, S., Mori, K., Yasuoka, N., Higuchi, Y*., et al.* (2010). Crystal structures of ethanolamine ammonia-lyase complexed with coenzyme B12 analogs and substrates. J. Biol. Chem. *285*, 26484-26493.

Sievers, F., Wilm, A., Dineen, D., Gibson, T.J., Karplus, K., Li, W., Lopez, R., McWilliam, H., Remmert, M., and Söding, J. (2011). Fast, scalable generation of high-quality protein multiple sequence alignments using Clustal Omega. Mol. Syst. Biol. *7*.

1169 Singh, S.B., and Lin, H.C. (2015). Hydrogen sulfide in physiology and diseases of the digestive
1170 tract. Microorganisms *3*, 866-889.

1171 Smith, E.A., and Macfarlane, G.T. (1998). Enumeration of amino acid fermenting bacteria in the
1172 human large intestine: effects of pH and starch on peptide metabolism and dissimilation of
1173 amino acids. FEMS Microbiol. Ecol. *25*, 355-368.

1174 Stoll, S., and Schweiger, A. (2006). EasySpin, a comprehensive software package for spectral
1175 simulation and analysis in EPR. J. Magn. Reson. *178*, 42-55.

1176 Terwilliger, T.C., Grosse-Kunstleve, R.W., Afonine, P.V., Moriarty, N.W., Zwart, P.H., Hung, L.W.,
1177 Read, R.J., and Adams, P.D. (2008). Iterative model building, structure refinement and density
1178 modification with the PHENIX AutoBuild wizard. Acta Crystallogr. D Biol. Crystallogr. *64*, 61-69.

1179 Tomasova, L., Konopelski, P., and Ufnal, M. (2016). Gut bacteria and hydrogen sulfide: The new
1180 old players in circulatory system homeostasis. Molecules *21*.

1181 Toraya, T. (2003). Radical catalysis in coenzyme B12-dependent isomerization (eliminating)
1182 reactions. Chem Rev *103*, 2095-2127.

1183 Xing, M., Wei, Y., Zhou, Y., Zhang, J., Lin, L., Hu, Y., Hua, G., A, N.N.U., Liu, D., Wang, F.*, et al.*
1184 (2019). Radical-mediated C-S bond cleavage in C2 sulfonate degradation by anaerobic bacteria.
1185 Nat. Commun. *10*, 1609.

1186 Yang, Z.Y., Mehmood, R., Wang, M.Y., Qi, H.W., Steeves, A.H., and Kulik, H.J. (2019). Revealing
1187 quantum mechanical effects in enzyme catalysis with large-scale electronic structure
1188 simulation. React. Chem. *4*, 298-315.

1189 Yazici, C., Wolf, P.G., Kim, H., Cross, T.W.L., Vermillion, K., Carroll, T., Augustus, G.J., Mutlu, E.,
1190 Tussing-Humphreys, L., Braunschweig, C.*, et al.* (2017). Race-dependent association of
1191 sulfidogenic bacteria with colorectal cancer. Gut *66*, 1983-1994.

1192 Zhou, Y., Wei, Y., Lin, L., Xu, T., Ang, E.L., Zhao, H., Yuchi, Z., and Zhang, Y. (2019). Biochemical
1193 and structural investigation of sulfoacetaldehyde reductase from Klebsiella oxytoca. Biochem. J.
1194 *476*, 733-746.
1195